https://doi.org/10.1016/j.compositesb.2021.108883

Two advantages by a single move: core-bishell electrode design for ultrahigh-rate capacity and ultralong-life cyclability of lithium ion batteries

Wenbo Liu,[a,*] Peng Xiang,[a] Xin Dong,[a] Huabing Yin,[b] Hua Yu,[c,*] Peng Cheng,[a] Shichao Zhang,[d] Sanqiang Shi[e]

[a] School of Mechanical Engineering, Sichuan University, Chengdu 610065, China

[b] Institute for Computational Materials Science, School of Physics and Electronics, Henan University, Kaifeng 475004, China

[c] Institute of Photovoltaics, Southwest Petroleum University, No. 8 Xindu Road, Chengdu 610500, China

[d] School of Materials Science and Engineering, Beihang University, Beijing 100191, China

[e] Department of Mechanical Engineering, The Hong Kong Polytechnic University, Hung Hom, Kowloon, Hong Kong 999077, China

Tel: +86-028-85405320; Fax: +86-028-85403408; E-mail: liuwenbo_8338@163.com.

Developing efficient electrodes with superior rate performance and superb cyclability are highly desired for meeting urgent demand of high-energy and large-rate lithium ion batteries (LIBs). Electrochemical performance of popular transition metal oxide electrodes is severely restricted by its inferior structure stability and low conductivity, leading to rapid capacity fade at high current density or deep cycling. Herein, a unique 3D core-bishell (3D-CBS) nanoporous electrode with configuration of Cu (NPC) core and bi-layered conformal Cu_2O@PANI shells was dedicatedly designed and built by a novel and cost-effective approach combining chemical dealloying with controlled electro-polymerization. The 3D-CBS nanoporous electrodes deliver a large reversible capacity of 349 mAh g^{-1} at 6000 mA g^{-1} after 11500 ultralong-cycles with 76% capacity retention, corresponding to only 0.002% capacity fade per cycle. The superb cyclability is related to the unique 3D-CBS electrode design and in-situ formation of Cu_2O with exposed most Cu^+ (Cu^+/O^{2-}=4/1) and low-energy (111) crystal plane (0.046 eV/Å^2) on NPC matrix, as confirmed by physicochemical characterization and DFT calculation. Impressively, the 3D-CBS electrode displays superior rate capability with negligible capacity fade after 5 multistep-rate periods from 2 up to 20 A g^{-1} and back again to 2 A g^{-1} repeatedly (over 400 cycles), which is ascribed to the conformal coating of PANI as protective nanolayers with good conductivity on Cu_2O, achieving ultrafast Li^+ diffusivity (D_{Li}=2.42×10^{-10} cm^2 s^{-1}) and significantly improved electron conductivity (82000 S m^{-1}). We believe that this work provides novel insights for design and synthesis of ultrahigh-rate and ultralong-life nanostructured anodes toward advanced LIBs.

Keywords: Ultrahigh-rate and ultralong-life anode; Core-bishell nanoporous structure; Lithium ion battery; Dealloying; DFT calculations

1. Introduction

Nowadays, the rapid development of mobile communication, hybrid/pure electric vehicles, and smart power grids evokes increasingly high demands toward high energy density and large rate lithium ion batteries (LIBs) [1,2]. However, graphite, as the most widely used commercial LIB anode material, is far too long to meet these demands due to its limited theoretical specific capacity (372 mAh g^{-1}) and relatively poor safety [3,4]. Thus, exploring and developing new cost-effective anode material with superb cyclability and excellent large rate performance is key to achieve new generation LIBs.

In 2000, Tarascon et al. firstly reported transition metal oxides (TMOs) as anode material for LIBs, exhibiting quite promising electrochemical performance [5]. Since then, numerous researches strived for substituting TMOs anode for graphite in commercial LIBs [6-10]. Unfortunately, until now, some inherent drawbacks of TMOs, such as large volume/structure variations [11-13], poor electron conductivity [14-16] and low coulombic efficiency, still cannot be well-solved and thus severely impeded their future applications [17-20].

To tackle these issues, some effective approaches have been proposed and employed in the past few years. Typically, designing nanostructured TMOs with large specific surface area and short mass transfer distance can effectively improve Li^+ migration kinetics and electrochemical reaction activity [21-23]. Among them, 3D nanoporous architecture has attracted great attention in LIBs because of enlarged contact surface area between electrode and electrolyte, shortened ion/electron

migration lengths as well as boosted porosity for loading of active material [21,24-27]. Especially, nanoporous metals (NPMs) have been investigated to serve as both substrates and/or current collectors of TMOs for high-performance LIBs, exhibiting superior electrochemical durability owing to effective accommodation for volume change by ample nanovoids and adequate buffering of mechanical strain by robust 3D porous skeleton [28-29]. The NPMs with different surface morphologies, pore sizes and distribution patterns can be fabricated by dealloying of various alloy systems (e.g. Cu-Mn, Au-Ag, Cu-Al and so forth) [10,30]. Evidently, compared to conventional three-dimensional nanoporous metals/transition metal oxides (3D-NPMs/TMOs) composite electrodes prepared by ex-situ routes, in-situ constructing freestanding 3D-NPMs/TMOs integrated electrodes with stronger binding force and better structure stability would be more desirable toward their practical application [24,31]. In addition, it has been known that conducting polymer coatings have a great advantage in improving electron conductivity of active material and enhancing coulombic efficiency by stabilizing solid electrolyte interface (SEI) membranes, as well as protecting structural integrity from pulverization and exfoliation [32-35]. For example, Cui et al. [35] reported a conducting polymer hydrogel combined with Si-based anode achieving 5000 long cycle life with over 90% capacity retention. As a result, it could be expected reasonably that uniform and conformal conducting polymer coatings incorporated into 3D-NPMs/TMOs integrated electrode with suitable pore sizes and distribution patterns would markedly enhance its conductivity and structure stability, leading to excellent electrochemical durability and long cycle

life.

In this paper, a freestanding 3D core-bishell nanoporous Cu@Cu_2O@polyaniline (3D-CBS NPC@Cu_2O@PANI) electrode has been prepared by a novel and cost-effective method in which the 3D core-shell nanoporous Cu@Cu_2O (3D-CS NPC@Cu_2O) integrated electrode stems from in-situ chemical dealloying and PANI nanolayer as the second shell from electro-polymerization. To the best of our knowledge, it is the first time to achieve nanoporous structure from binary Cu-Sn system with notably narrow standard reversible potential difference by simple one-step chemical dealloying. The prepared nanoporous electrodes for LIBs exhibit excellent electrochemical performance of superb cycling stability and superior rate capability. It is believed that this work can pave a golden road for design and construction of promising high-performance nanostructured anodes toward advanced LIBs.

2. **Results and discussion**

2.1. Microstructure and Morphology Characterization

The preparation processes of freestanding 3D-CS NPC@Cu_2O and 3D-CBS NPC@Cu_2O@PANI electrodes is illustrated in Figure 1a. Briefly, the freestanding 3D-CS NPC@Cu_2O electrode is fabricated in-situ by one-step chemical dealloying of as-casted $Cu_{65}Sn_{35}$ slices in mixed corrosive solution of HF and HNO_3 at 90℃ for 5 hrs. It is known that complete dealloying for Cu-Sn alloy system with narrow reversible potential difference (less than 500 mV, -0.136 V for Sn/Sn^{2+} vs. SHE and 0.342 V for Cu/Cu^{2+} vs. SHE) [36]. However, it is inspiring that complete dealloying

was successfully achieved by a simple one-step chemical dealloying in this approach. Subsequently, the freestanding 3D-CBS NPC@Cu_2O@PANI electrode is attained further by controlled electro-polymerization of aniline on the 3D-CS NPC@Cu_2O electrode to improve the structure stability and conductivity.

Figure 1b-c show the surface and cross-section SEM images of 3D-CS NPC@Cu_2O electrode, respectively. As can be seen from Figure 1b, the topographic view of the 3D-CS electrode exhibits open, bicontinuous interpenetrating networks with typical sizes of 800±200 nm (pore) and 300±150 nm (ligament), respectively. All the ligaments are noted with smooth outer surface and sharp corner angle. The cross-section view of the 3D-CS electrode further displays that the bicontinuous interpenetrating porous network throughout the whole specimen, indicating that the as-obtained nanoporous structure is homogeneous (Figure 1c). EDX analysis shows that both Cu and O elements are detected in the resultant products, suggesting the formation of copper(I/II) oxide upon dealloying (Figure S1). Figure 1d-e present the surface and cross-section SEM images of 3D-CBS electrode. Clearly, the as-synthesized 3D-CBS electrode well inherits the microstructure network and porosity of the 3D-CS electrode. However, the wrinkled surface patterns and softly rounded corners are clearly observed on the ligaments, which are quite different from the observation before electro-polymerization, implying the favorable coverage of PANI layer on the 3D-CS electrode. Additionally, EDX results revealed that aside from Cu and O, C and N elements also exist in the 3D-CBS products, confirming that PANI was successfully deposited on the 3D porous skeleton (Figure S2). Furthermore,

there are no obvious surface cracking, pulverization and detachment either in the 3D-CS or the 3D-CBS nanoporous electrodes, suggesting the good structural integrity which could facilitate advanced LIBs.

TEM observation (Figure 1f and its inset) further shows the uniform nanosized ligament-pore structure and conformal Cu_2O shell with thickness of ~5 nm can be discerned clearly on the ligament surfaces of 3D-CS electrode, indicative of in-situ formation of core-shell nanoporous architecture. The HRTEM analysis (Figure 1g) reveals that the lattice fringe spacings of surface nanoshell and inner nanocore in the 3D-CS integrated electrode are 2.46 Å and 2.08 Å, respectively, assigning to the (111) plane of Cu_2O and the (111) plane of Cu, implying the good in-situ growth of Cu_2O nanoshell on the ligament surfaces of NPC matrix during dealloying. The corresponding SAED pattern (inset of Figure 1g) exhibits the typical polycrystalline diffraction image, further confirming the existence of Cu and Cu_2O. To understand the formation mechanism of the 3D-CS integrated electrode, briefly, on one hand, the component Sn in the Cu-Sn alloy serving as an anode preferentially dissolves into the mixed solution and the remaining Cu atoms will rearrange to form nanoporous structure with uniform pore size distribution by rapid surface diffusion along the alloy/solution interfaces [36]; on the other hand, the dissolved active oxygen radical (·O) in the corrosive solution can be captured quickly by activated superficial Cu atoms with unsaturated bonds and high surface energy to further forming Cu_2O nanoshell on ligament surfaces of NPC matrix via in-situ growth so that the system keeps low free energy state. It is worth noting that Cu_2O nanoshell can retain

relatively stable in the acid as long as Sn has not yet been etched totally because H^+ in the acid would preferentially react with Sn with higher electrochemical activity. Moreover, HRTEM images of the 3D-CBS nanoporous electrode after electro-polymerization further show a uniform PANI layer with thickness of ~5 nm coated on Cu_2O nanoshell, in which no lattice fringes can be observed, indicating the amorphous nature of PANI nanolayer (Figure 1h). Thus, based on the characterizations, it is confirmed that the unique 3D core-bishell NPC@Cu_2O@PANI electrode was successfully fabricated with a novel and cost-effective approach. The Brunner-Emmet-Teller (BET) measurement was further carried out by N_2 adsorption-desorption experiment (Figure S3). The specific surface area of the 3D-CBS NPC@Cu_2O@PANI electrodes is 1.14 m^2 g^{-1}, which is favorable for enlarging the contact area between active materials and electrolyte, resulting in high Li storage capacity. The electronic conductivity of 3D-CS and 3D-CBS electrodes was also tested using four-point probe method (see Note 1 in the Supplementary Material for measurement details). Obviously, the 3D-CBS electrode (82000 S m^{-1}) has higher electronic conductivity compared to 3D-CS electrode (24200 S m^{-1}), suggesting that the PANI coatings effectively facilitate the electron transport network.

Figure 2a displays the XRD patterns of the as-cast $Cu_{65}Sn_{35}$ alloy, as-synthesized 3D-CS and 3D-CBS nanoporous electrodes, respectively. The initial $Cu_{65}Sn_{35}$ alloy is composed of two phases: Cu_6Sn_5 (ICDD No. 45-1488) and Cu_3Sn (ICDD No. 01-1240), in which the amount of Cu_6Sn_5 is comparable to that of Cu_3Sn. Upon dealloying, three main diffraction peaks at 2θ=43.2°, 50.4° and 74.1° correspond to

f.c.c $(111)_{Cu}$, $(200)_{Cu}$ and $(220)_{Cu}$ respectively, confirming the existence of Cu phase; meanwhile, Cu_2O phase is also detected at $2\theta=36.4°$, suggesting the co-existence of Cu and Cu_2O in the as-dealloyed products [10,31]. For the 3D-CBS nanoporous electrode, more diffraction peaks of Cu_2O are clearly observed at $2\theta=29.5°$, 42.2° and 61.3° which is owing to surface oxidation of NPC during electro-polymerization [37]. In addition, chemical compositions and surface valence states of the 3D-CS and 3D-CBS nanoporous electrodes were also characterized by XPS measurement. As presented in Figure 2b, only Cu and O elements can be identified in the as-dealloyed products, while Cu, O, C and N can be detected simultaneously in the as-electropolymerized products, further confirming the successful deposition of PANI nanolayer upon the 3D-CS electrode. The high-resolution XPS spectra (Figure 2c) of Cu 2p for the 3D-CS and 3D-CBS nanoporous electrodes display that the binding energies of Cu $2p_{1/2}$ and Cu $2p_{3/2}$ located at 952.18 and 932.28 eV respectively, clearly indicating the existence of Cu(I) rather than Cu(II) in the fabricated specimens [37-39]. Furthermore, Raman spectroscopy was also employed to inspect the chemical structures of the 3D-CS and 3D-CBS nanoporous electrodes. As shown in Figure 2d, the Raman spectrum of the 3D-CS electrode exhibits two main peaks at 525 and 615 cm^{-1}, corresponding to the T_g and B_g modes of Cu_2O, respectively [40,41]. In contrast, the counterpart of the 3D-CBS nanoporous electrode reveals more peaks of PANI at 1165, 1245, 1390, 1494 and 1595 cm^{-1}, which is well designated to C-H bending mode of quinoid/benzenoid rings, weak C-H, C-N and C=N stretching modes of quinoid ring, as well as C-C stretching mode of benzenoid ring, respectively [23,42].

Overall, based on the characterizations above, it is concluded that the 3D-CS and 3D-CBS electrodes are successfully fabricated by facile method combining one-step chemical dealloying with post-electro-polymerization in this work.

2.2. Electrochemical properties

In order to evaluate the electrochemical performance, the as-prepared 3D-CS and 3D-CBS electrodes were served as anodes assembled into LIB half-cells without using binder and conductive agent. In comparison, 2D planar copper foil (CF) supported Cu_2O nanoparticles (2D CF@Cu_2O NPs) electrodes were also fabricated by simple two-step heat treatments of 2D CF in air at 550℃ for 1 h and then in N_2 atmosphere at 700℃ for 2 h (see Supplementary Material, Figures S4-S5). Figure 3a shows the CVs of 3D-CBS electrode with potential range of 0.01 to 3.0 V (vs. Li/Li^+) at a scan rate of 0.1 mV s^{-1}. Clearly, during the first discharge process, the reduction peaks centered at 1.0 and 0.37 V (vs. Li/Li^+) can be ascribed to the transformation of Cu_2O to Cu ($Cu_2O + 2Li^+ + 2e^- \rightarrow 2Cu + Li_2O$) and formation of SEI membranes, respectively [8,19]. For the first charge process, three main anodic peaks locate at 0.6, 1.4 and 2.54 V (vs. Li/Li^+), which can be attributed to the partial decomposition of SEI membranes and stepwise reverse transformation of Cu to Cu_2O ($Li_2O + 2Cu \rightarrow Cu_2O + 2Li^+ + 2e^-$) [9,21,37]. Note that during the following discharge processes, the initial broad cathodic peak divides into three counterparts centered at 1.63, 1.11 and 0.82 V (vs. Li/Li^+) respectively, which is closely related to the size change of partial Cu_2O caused by nano-crystallization during the first transformation, resulting in the higher shift of its lithiation potential and the increase of potential difference [10,37].

Compared to the 2D planar copper foil supported Cu_2O nanoparticles (2D CF@Cu_2O NPs) electrode (Figure S6), the 2nd and 3rd CVs of the 3D-CBS nanoporous electrode are well overlapped with each other, indicating its superior electrochemical reversibility and cycling stability.

Figure 3b shows the potential vs. capacity profiles of 3D-CBS electrode ranging from 0.01 to 3.0 V (vs. Li/Li^+), in which the initial three cycles run at a low current density (200 mA g^{-1}) for electrode activation related to the higher one (2 A g^{-1}) in the following cycles. Surprisingly, the first discharge and charge processes delivered superb large specific capacities of 1411 and 677 mAh g^{-1} with ca. 48% coulombic efficiency. It has been known that pure PANI can only deliver limited Li storage capacity of ca. 20 mAh g^{-1}, and its capacity contribution can be ignored as used in the high-capacity electrode materials [33,35]. The achieved capacity is far beyond the theoretical value of Cu_2O (374 mAh g^{-1}), which could be due to the repeated formation and decomposition of SEI membranes (in good line with the CVs) as well as the unique 3D-CBS nanoporous structure with more electrochemical active sites in favor of Li^+ storage than conventional micron-sized counterparts [43]. Actually, this phenomenon has been found widely in various nanostructured Cu_2O electrode materials in the literature [9,44-47]. Moreover, the initial capacity loss is mainly ascribed to the incompletely reversible conversion of Cu_2O, partial decomposition of SEI membranes as well as occurrence of a series of irreversible side reactions on the electrode surfaces, such as reductions of superficial contaminants or adsorbed species [31,48]. Single broad discharge plateau at ~1.2 V (vs. Li/Li^+) changes into two

counterparts just after the 1st cycle, which is in good agreement with the CVs in Figure 3a. Furthermore, the 2nd charge-discharge profile with two potential plateaus overlaps well with the 3rd cycle and even if under the higher current density (2 A g^{-1}), the 4th and 100th charge-discharge profiles also overlap well with each other, further demonstrating the excellent electrochemical reversibility of the unique 3D-CBS nanoporous electrode.

Cycling stability is one of the key indexes to assess the electrochemical properties of LIBs. Figure 3c illustrates the cycling performance of 2D CF@Cu_2O NPs, 3D-CS NPC@Cu_2O and 3D-CBS NPC@Cu_2O@PANI electrodes at 2 A g^{-1}, in which the initial three cycles run at a low current density (200 mA g^{-1}) for electrode activation. It is shown that compared to the 2D CF@Cu_2O NPs electrode, both the 3D-CS and 3D-CBS nanoporous electrodes display the remarkably improved cycling abilities with higher specific capacity, and coulombic efficiency. This indicates that the 3D nanoporous configuration is greatly beneficial for enhancing the loadings of active material and alleviating the volume and structure variations during cycling. Prominently, the unique 3D-CBS nanoporous electrode exhibits ultrahigh first reversible capacity of 555 mAh g^{-1} at 2 A g^{-1} and superior cycling stability with ~111% capacity retention after 300 cycles. The typical reversible capacities of 563, 559, 549 and 567 mAh g^{-1} was achieved for the 10th, 50th, 100th and 150th cycles, respectively; after 300 cycles, it still delivers an ultrahigh reversible capacity of 621 mAh g^{-1} with zero capacity loss in comparison with the 1st cycle at 2 A g^{-1}. Moreover, the coulombic efficiency demonstrates negligible fade, maintaining over 99.5% of its

initial value after 300 cycles. This usual phenomenon in TMOs electrodes strongly indicates the superior electrochemical reversibility of 3D-CBS nanoporous electrodes. It is noticed that a slight increase of specific capacity occurs during repeated charge-discharge processes for the 3D-CBS nanoporous electrodes, which is ascribed to the enlarged reaction sites with abundant pores/diffusion channels during the process of reversible formation and decomposition of a polymeric gel-like layer [8,10]. In contrast, for the 2D CF@Cu_2O NPs electrode, the reversible capacities of 198, 66 and 63 mAh g^{-1} is obtained for the 1^{st}, 5^{th} and 50^{th} cycles, respectively. There is a sharp decrease after 50 cycles, suggesting its poor cycling stability. This is closely associated with the planar structure and compact stacking of Cu_2O NPs, leading to inadequate buffering of volume change and mechanical strain during repeated lithiation-delithiation processes as well as rapid exfoliation of active material from the surfaces of 2D CF substrate.

The long-term cycling stability of 3D-CBS electrode at higher current densities of 4 and 6 A g^{-1} was further examined, as indicated in Figure 3d-e. After electrode activation with 3 cycles, the 3D-CBS nanoporous electrode exhibits ultrahigh reversible capacity of 518 mAh g^{-1} at 4 A g^{-1} and outstanding cycling ability with ~105% capacity retention and 99.8% coulombic efficiency after 800 cycles. Excitingly, with current density up to 6 A g^{-1}, a relatively high reversible capacity of 349 mAh g^{-1} still can be achieved with ~76% capacity retention after 11500 ultralong-cycles, corresponding to only 0.002% capacity decay per cycle. Moreover, slight capacity decays are observed from the potential vs. capacity curves (Figure S7)

with no obvious potential plateau changes during the ultralong charge-discharge processes, further confirming its superb cyclability. It is worth mentioning that the steady reversible capacity of 386 mAh g^{-1} after 8000 cycles at 6 A g^{-1} is still greater than the theoretical specific capacity of commercial graphite anode (372 mAh g^{-1}), suggesting its considerably promising application in advanced LIBs.

It is well-recognized that rate capability is another important evaluation for electrochemical performance of LIBs. Herein, the 5 multistep-rate programmed tests (total over 400 cycles) were carried out from 2 up to 20 A g^{-1} and then back to 2 A g^{-1}, in which each period comprises 8 steps and each step runs 10 cycles under different current densities. Figure 3f displays the rate capability profiles of 3D-CBS electrode based on the designed test procedure. As indicated clearly in the 1^{st} multistep-rate period, the high reversible capacities of 542, 462, 400, 329 and 283 mAh g^{-1} is delivered at current densities of 2, 6, 10, 16 and 20 A g^{-1}, respectively. When current density returns to its initial values (16, 10, 6 and 2 A g^{-1}) at the 51^{th}, 61^{th}, 71^{th} and 81^{th} cycles step by step, the reversible capacity increases to 289, 336, 393 and 498 mAh g^{-1} accordingly, which reserves as high as 87.8%, 84%, 85.1% and 91.9% capacity retentions compared with the 31^{th}, 21^{th}, 11^{th} and 1^{st} cycles at same current densities, respectively. Surprisingly, after 5 continuous multistep-rate periods by the same test procedure, no obvious capacity decay can be observed at the 410^{th} cycle at 2 A g^{-1} (540 mAh g^{-1}). Meanwhile, the potential vs. capacity profiles at 20 A g^{-1} designed in each multistep-rate period are illustrated in Figure 3g. The charge-discharge curves for the 50^{th}, 130^{th}, 210^{th}, 290^{th} and 370^{th} cycles overlap with each other (including

their variation trend, potential plateau, and specific capacity), fully manifesting the ultrafast and ultra-stable kinetic characteristics for electrochemical lithiation/delithiation reactions on electrode interfaces. The scattergram in Figure 3h summarizes the typical reversible capacity values at the lowest (2 A g^{-1}) and highest (20 A g^{-1}) current densities, respectively. It is apparent that the reversible capacities stabilize at around 540 and 280 mAh g^{-1} with nearly 100% capacity retentions at 2 and 20 A g^{-1} regardless of increasing rate periods and cycle numbers, indicating its superior cycling ability even if under such rigorous rate conditions. Furthermore, after undergoing a series of successive high-rate charge-discharge cycles from 2 to 12 A g^{-1}, the reversible capacity maintains as high as 467 mAh g^{-1} after 800 cycles with nearly zero capacity loss at a fixed current density of 6.6 A g^{-1}, implying its extreme excellence for rate performance (Figure 3i). This can be mainly attributed to the unique 3D-CBS nanoporous architecture and large contact areas between electrode and electrolyte, which can not only accommodate the huge volume change and endow good electrolyte permeation, but also facilitate the Li^+ migration during rapid charge-discharge processes. Meanwhile, the uniform and conformal PANI coating on Cu_2O surfaces can enhance the SEI stability and improve the electrode conductivity, which can remarkably boost the charge transfer efficiency for a better rate performance. The cyclability at high-rate of the 3D-CBS nanoporous electrode is evidently better than those of Cu-based oxides and their composites reported so far as illustrated in Figure 3j (see detailed experimental data and related references in Table S1).

To further investigate the excellent rate performance, the capacitive contribution of 3D-CBS NPC@Cu_2O@PANI electrode was calculated according to a series of CVs at different scan rates. Figure 4a displays the CVs of 3D-CBS NPC@Cu_2O@PANI electrode from 0.2 to 3.0 mV s^{-1}. The degree of capacitance effect can be qualitatively analyzed from CVs through the relationship between current (i) and scan rate (v): $i = av^b$, where both a and b are constants [49,50]. The b value can be determined from the slope of the log(i) *versus* log(v) plot (Figure 4b), which is always between 0.5 and 1.0. As b=0.5, the current response is diffusion-controlled; as b=1, the current is controlled by capacitive process. In this case, the b value ranges from 0.74 to 0.86, indicating that the electrochemical reaction of the 3D-CBS nanoporous electrode was dominated by capacitive process. To further analyze the contribution of capacitance, the current respond can be separated to capacitive (k_1v) and diffusion-controlled processes ($k_2v^{0.5}$) [51-53]:

$$i\,(V)=k_1v+k_2v^{0.5} \quad (1)$$

$$i\,(V)/v^{0.5}=k_1v^{0.5}+k_2 \quad (2)$$

Where both k_1 and k_2 are constants and v is the scan rate. Clearly, a high capacitive contribution of 71.06% is obtained at a scan rate of 2.0 mV s^{-1}, as shown in Figure 4c. With the increase of scan rate, the contribution of capacitance gradually increases and a maximum contribution value of 77.62% is obtained at the scan rate of 3.0 mV s^{-1} (Figure 4d). The results demonstrate that the pseudocapacitive process exists in the electrochemical reaction of 3D-CBS NPC@Cu_2O@PANI electrode, which is largely beneficial to the superior rate performance.

The ion and electron transfer characteristics of 3D-CS and 3D-CBS electrodes were investigated by EIS measurement. As can be seen from Figure 5a and b, all Nyquist plots consist of a compressed semicircle in high-medium frequency range, the diameter of which represents the charge transfer resistance (R_{ct}) and an inclined line in low frequency range closely related to the diffusion coefficient of Li^+ inside electrode materials, respectively [4,10]. Clearly, the R_{ct} of the 3D-CBS nanoporous electrode is ca. 140 Ω before cycling and decreases to just ca. 80 Ω after 300 cycles, which is mainly due to the dispersion distribution of generated Cu nanoparticles with good conductivity in amorphous Li_2O and continual permeation of electrolyte during charge-discharge processes [31,37]. Amazingly, after 11500 ultralong-cycles, the R_{ct} value is still as low as ca. 120 Ω, comparable to its initial state before cycling, confirming its outstanding electronic conductivity (Figure 5a). The R_{ct} of the 3D-CS integrated electrode is ca. 220 and 300 Ω before and after cycling respectively, slightly larger than the 3D-CBS nanoporous electrode (Figure 5b). In contrast, the R_{ct} values of the 2D planar electrode is much larger no matter before or after cycling (ca. 380 and 820 Ω, Figure S8), demonstrating the superior electron transfer abilities in the 3D CS-typed porous electrodes. To further understand their kinetic properties during electrochemical lithiation-delithiation reactions, the Li^+ diffusivity in the 3D-CS and 3D-CBS electrodes is evaluated using the following equation [54-56].

$$D = \frac{R^2T^2}{2A^2n^4F^4C^2\sigma_\omega^2} \quad (3)$$

Where R, T, A, n, F and C refer to gas constant, absolute temperature, geometric surface area of electrode, the number of electrons in electrochemical reaction, Faraday

constant and concentration of lithium ion, respectively. The Warburg impedance coefficient (σ_ω) can be obtained from the slope of real part (Z') vs. angular frequency ($\omega^{-1/2}$) profile in low frequency range, as depicted in Figure 5c and d. As a result, the Li^+ diffusion coefficients inside the 3D-CS and 3D-CBS nanoporous electrodes before and after cycling were estimated by Eqn. (3), as listed in detail in Table 1. Obviously, the 3D-CBS electrode has a relatively large Li^+ diffusion coefficient (5.52×10^{-11} cm^2 s^{-1}) at its initial state compared to that of the 3D-CS electrode (1.29×10^{-11} cm^2 s^{-1}). Moreover, the Li^+ diffusion coefficient of the 3D-CBS electrode exhibits an evident increase after 300 cycles (24.20×10^{-11} cm^2 s^{-1}), much greater than that of the 3D-CS electrode (0.15×10^{-11} cm^2 s^{-1}). It is exciting that a relatively large Li^+ diffusion coefficient (1.77×10^{-11} cm^2 s^{-1}) still can be reached even after 11500 ultralong-cycles in the 3D-CBS electrode, comparable to that of the 3D-CS electrode before cycling, suggesting the faster Li^+ diffusivity in the 3D-CBS nanoporous electrode. This is ascribed to the in-situ formation of active material on porous matrix and conformal coating of PANI nanolayer with good conductivity on active material, which is in great favor of reducing the contact resistance at the electrode/electrolyte and current collector/active material interfaces, shortening the Li^+ migration distance inside electrode material, as well as improving the electron conductivity.

Figure 6 illustrates the SEM images of 2D CF@Cu_2O NPs, 3D-CS NPC@Cu_2O and 3D-CBS NPC@Cu_2O@PANI electrodes after cycling. For the 2D CF@Cu_2O NPs electrode after 300 cycles, many irregular micro-flakes, comprising agglomerated nanoparticles and large-sized concave pits caused by severe cracking, pulverization

and detachment of active material, can be observed in Figure 6a and its inset, which is significantly different from its pristine state in Figure S4a. Especially, the disappearance of independent NPs after cycling indicates that the 2D planar substrate structure cannot effectively alleviate the huge volume change during charge-discharge processes, leading to terrible electrochemical performance. Moreover, the microstructure of 3D-CS NPC@Cu_2O electrode after 300 cycles was displayed in Figure 6b. The 3D bicontinuous porous network was well reserved after cycling, whereas the disordered orientation and uneven distribution of ligaments and pores suggest partial accommodation of volume expansion and contraction during reduplicative electrochemical reactions, resulting in the acceptable structure stability and electrochemical behavior. In contrast, SEM images of 3D-CBS electrode after 300 cycles in Figure 6c showed no evident discrepancy before and after cycling. The higher-magnification SEM image (inset in Figure 6c) further reveals the perfect 3D porous architecture with homogeneous ligament-pore distribution and benign structural integrity after cycling, implying its excellent electrochemical durability. To further verify the superiority of the 3D-CBS nanoporous electrode, its microstructure after 11500 ultralong-cycles at an elevated current density (6 A g^{-1}) was also characterized, as illustrated in Figure 6d. It is astonishing that the 3D-CBS configuration is well reserved with slightly thicker SEI membranes observed. There is no presence of cracking, pulverization and exfoliation of active material at all, fully demonstrating its superb structural integrity and electrochemical stability toward practical application of advanced LIBs.

Herein, the 3D-CBS NPC@Cu_2O@PANI//$LiCoO_2$ Li-ion full cell was assembled further by using the 3D-CBS nanoporous electrode and commercial $LiCoO_2$ electrode as cathode. As indicated in Figure 7, the electrochemical performance of 3D-CBS NPC@Cu_2O@PANI//$LiCoO_2$ full cell was investigated in the voltage range of 0.5-3.8 V. Figure 7a shows its cycle performance curves with intermittent rate measurements. Clearly, the initial discharge process (Li^+ migration from the 3D-CBS anode to $LiCoO_2$ cathode) delivered a high reversible capacity of 477 mAh g^{-1} with ~51% coulombic efficiency. The first discharge capacity loss is closely related to the incomplete reversible conversion of Cu_2O and formation of SEI membranes. Except for the first several cycles, the coulombic efficiency always maintains over 98%, indicating its favorable electrochemical reversibility. Impressively, the discharge specific capacities of 330, 330, 311 and 299 mAh g^{-1} can be obtained in sequence at a current density of 2 A g^{-1} for the 100^{th}, 1000^{th}, 1500^{th} and 2000^{th} cycles with capacity retentions of 70%, 70%, 65% and 63%, respectively. Even after 3000 ultralong-cycles, a relatively large discharge capacity of 315 mAh g^{-1} still can be reached smoothly, reserving as high as 66% capacity retention and 99.7% coulombic efficiency, suggesting its excellent cycle performance including good cycling stability and ultralong cycle life. Like the half-cells, a slight increase of capacity during cycling is related to the unceasing permeation of organic electrolyte and wetting of 3D porous electrode in the full cells. Figure 7b-d shows the intermittent rate capability profiles of 3D-CBS full cell, which were recorded from the 1^{st} to 50^{th} cycles, from the 1040^{th} to 1090^{th} cycles, and from the 2080^{th} to 2130^{th} cycles, respectively. As indicated in

Figure 7b, the relatively high discharge capacities of 378, 277, 228 and 196 mAh g^{-1} can be attained after each 10 cycles at 2, 4, 6 and 8 A g^{-1}, respectively. When the current density reverted to 2 A g^{-1} again, the discharge capacity increased to 313 mA h g^{-1}, maintaining as high as 82.8% capacity retention relative to that of the 10^{th} cycle at the same current density. Analogically, in Figure 7c and d, the discharge capacities of 315 and 286 mA h g^{-1} can be achieved for the 1081^{th} and 2021^{th} cycles at 2 A g^{-1} after a series of high-rate, long-term lithiation-delithiation processes, retaining 95.7% and 95.6% capacity retentions compared to those of the 1050^{th} and 2090^{th} cycles at same current densities, confirming its outstanding rate performance in full cells. Figure 7e-h displays the voltage vs. capacity curves of full cell under different current densities. Surprisingly, even if undergoing considerably long cycles, all the charge and discharge capacities decrease limitedly, bringing about relatively high capacity retentions at fixed current densities (2, 4, 6, even 8 A g^{-1}). In fact, apart from slight capacity loss, the shape, voltage plateau and variation trend of all voltage vs. capacity profiles under various current densities are similar, indicating the superior electrochemical reversibility and cycling stability of full cells, especially at high rates. For practical applications, a light-emitting-diode (LED) bulb powered by the assembled Li-ion full cell with full-charged state after 3000 cycles was exhibited in Figure 7i. Excitingly, after such a high-rate and ultralong charge-discharge cycles, the light radiation of LED bulb is still considerably strong and bright, which is encouraging for applications towards household/industrial microelectronic devices.

Compared to the 2D CF@Cu_2O NPs and other 3D nanostructured Cu-based oxides

electrodes reported so far, the superior electrochemical performance of the 3D-CBS electrode designed in this work demonstrates its intrinsic advantages of synergistic effect among the unique 3D-CBS nanoporous structure, large contact areas between active material and electrolyte, in-situ formation of active material on porous matrix, and conformal coating of protective layer with good conductivity on active material, which is illustrated schematically in Figure 8a. Firstly, the unique 3D-CBS nanoporous structure with large specific surface area and bicontinuous porous network can effectively accommodate large volume variation and offer efficient ion/electron transport channels during charge-discharge processes, resulting in stable cycling ability and long cycle life [57-60]. Secondly, large contact surface areas between active material and electrolyte facilitate to provide more active sites for lithiation-delithiation reactions and shorten Li^+ migration distance between electrode and electrolyte, bringing about the high rate capability. Thirdly, in-situ formation of uniform Cu_2O films with thickness in nanoscale on porous matrix can cause relatively small mechanical strain associated with volume expansion during lithiation reactions, as well as ensure strong mechanical adhesion and good electric contact between active material and current collector without any binder and conductive agent, which are essential in current commercial LIBs but inevitably cause the depressed energy and power densities. Fourth, the conformal coating of PANI protective layer with good conductivity on active material can not only significantly improve the electron conductivity and decrease the charge transfer resistance inside the electrode, but also effectively stabilize the SEI membranes to prevent active material from pulverization

and detachment from current collector surfaces. Besides, to deeply understand its superiority in lithium storage properties from the perspective of crystallography, density functional theory (DFT) calculations were further carried out (see Note 2 in the Supplementary Material for computational details of DFT). Figure 8b displays the 3D and 2D surface atomic configurations in different planes of Cu_2O unit cell, in which the (111) plane is the close-packed plane of atoms and contains more Cu^+ than other surfaces (Cu^+/O^{2-}=4/1 in the (111) plane). According to the positive linear relationship between the lithium storage properties of Cu_2O and the redox reaction of Cu^+/Cu^0 ion pair, the Cu_2O nanolayer with more exposed (111) planes could induce the occurrence of more and faster redox reaction of Cu^+/Cu^0 ion pair, resulting into higher reversible capacity and better rate capability. Also, the surface energy (E_s) in different planes of Cu_2O unit cell has been estimated based on the DFT models, as listed in Figure 8b. The (111) plane possesses the lowest surface energy (just 0.046 $eV/Å^2$), indicating much better stability than other planes as exposed to surfaces, leading to the better cycle performance. Therefore, the unique 3D-CBS nanoporous electrode with rational design endow itself excellent electrochemical performance, indicative of a promising TMOs-based anode candidate with ultrahigh-rate and ultralong-life lithium storage properties towards practical application of advanced LIBs.

3. Conclusions

A unique freestanding 3D core-bishell nanoporous electrode was developed with single NPC core and bi-layered conformal Cu_2O@PANI shells by combining

chemical dealloying with controlled electro-polymerization. The unique 3D-CBS nanoporous electrode as anode for LIBs exhibits excellent electrochemical performance with ultrahigh reversible capacity, ultralong cycle life and superb rate capability. This is closely associated with the rational design with controlled materials configuration, in-situ formation of active material on porous matrix, and conformal coating of protective nanolayer with good conductivity on exposed low-energy crystal plane with most Cu^{+} of active material. These features are largely beneficial to alleviating the huge volume/structure changes during lithiation-delithiation processes, strengthening the mechanical adhesion between active material and current collector, enhancing the solid electrolyte interface stability and structural integrity, shortening the Li^{+} diffusion distance and improving the electron conductivity. It is believed that this work has significant implication for span-new design and preparation of ultrahigh-rate, ultralong-life 3D nanostructured anodes toward advanced electrochemical energy storage devices.

Declaration of competing interest

The authors declare no competing financial interests.

Acknowledgements

We give thanks to financial support by the National Natural Science Foundation of China (52075351, 51604177), the National Key Research and Development Program of China (2019YFA0705701), the International S&T Innovation Cooperation Program of Sichuan Province (2020YFH0039), the Chengdu International S&T Cooperation Funded Project (2019-GH02-00015-HZ, 2020-GH02-00006-HZ), the “1000 Talents

Plan" of Sichuan Province, the Experimental Technology Project of Sichuan University (SCU201078), and the Talent Introduction Program of Sichuan University (YJ201410). Additionally, the authors specially thank Dr. Shanling Wang (Analytical & Testing Center, Sichuan University) for help in TEM characterization.

Author contributions

Wenbo Liu directed the project and designed the experiments. Peng Xiang, Xin Dong and Peng Cheng carried out the experiments and analyzed the data. Huabing Yin conducted the DFT simulation. Wenbo Liu wrote the main manuscript text and Hua Yu optimized it. Shichao Zhang and Sanqiang Shi added useful advice. All authors discussed the results and reviewed the manuscript.

Appendix A. Supplementary data

Supplementary data to this article can be found online at

Data availability

The data that support all plots within this paper is available from the corresponding author upon reasonable request.

References

[1] Armand M, Tarascon J-M. Building better batteries. Nature 2008;451:652-7.

[2] Nitta N, Wu FX, Lee JT, et al. Li-ion battery materials: present and future. Mater Today 2015;18(5):252-64.

[3] Meng JS, Guo HC, Niu CJ, et al. Advances in structure and property optimizations of battery electrode materials. Joule 2017;1(3):1-26.

[4] Grey CP, Tarascon J-M. Sustainability and in situ monitoring in battery

development. Nat Mater 2016;16(1):45-56.

[5] Poizot P, Laruelle S, Grugeon S, et al. Nano-sized transition-metal oxides as negative-electrode materials for lithium-ion batteries. Nature 2000;407(6803):496-9.

[6] Yu Y, Shi Y, Chen CH. Nanoporous cuprous oxide/lithia composite anode with capacity increasing characteristic and high rate capability. Nanotechnology 2007;18(5):005706.

[7] Lou XW, Deng D, Lee JY, et al. Self-supported formation of needlelike Co_3O_4 nanotubes and their application as lithium-ion battery electrodes. Adv Mater 2008;20(2):258-62.

[8] Park JC, Kim J, Kwon H, et al. Gram-scale synthesis of Cu_2O nanocubes and subsequent oxidation to CuO hollow nanostructures for lithium-ion battery anode materials. Adv Mater 2009;21(7):803-7.

[9] Xiang JY, Wang XL, Xia XH, et al. Enhanced high rate properties of ordered porous Cu_2O film as anode for lithium ion batteries. Electrochim Acta 2010;55(17):4921-5.

[10] Liu DQ, Yang ZB, Wang P, et al. Preparation of 3D nanoporous copper-supported cuprous oxide for high-performance lithium ion battery anodes. Nanoscale 2013;5(5):1917-21.

[11] Balogun MS, Wu ZP, Luo Y, et al. High power density nitridated hematite (α-Fe_2O_3) nanorods as anode for high-performance flexible lithium ion batteries. J Power Sources 2016;308:7-17.

[12] Taberna PL, Mitra S, Poizot P, et al. High rate capabilities Fe_3O_4-based Cu

nano-architectured electrodes for lithium-ion battery applications. Nat Mater 2006;5(7):567-72.

[13] Xiang JY, Tu JP, Yuan YF, et al. Improved electrochemical performances of core-shell Cu_2O/Cu composite prepared by a simple one-step method. Electrochem Commun 2009;11(2):262-5.

[14] Wang JX, Zhang QB, Lia XH, et al. Smart construction of three-dimensional hierarchical tubular transition metal oxide core/shell heterostructures with high-capacity and long-cycle-life lithium storage. Nano Energy 2015;12:437-46.

[15] Guo WX, Sun WW, Wang Y. Multilayer CuO@NiO hollow spheres: microwave-assisted metal-organic-framework derivation and highly reversible structure-matched stepwise lithium storage. ACS Nano 2015;9(11):11462-71.

[16] Liang P, Zhang HG, Su YB, et al. In-situ preparation of binder-free nano-cotton-like CuO-Cu integrative anode on current collector by laser ablation oxidation for long cycle life li-ion batteries. J Mater Chem A 2017;5(37):19781-9.

[17] Rehnlund D, Valvo M, Tai CW, et al. Electrochemical fabrication and characterization of Cu/Cu_2O multi-layered micro and nanorods in Li-ion batteries. Nanoscale 2015;7(32):13591-604.

[18] Subalakshmi P, Sivashanmugam A. CuO nano hexagons, an efficient energy storage material for Li- ion battery application. J Alloys Compd 2017;690:523-31.

[19] Hu L, Huang YM, Zhang FP, et al. CuO/Cu_2O composite hollow polyhedrons fabricated from metal-organic framework templates for lithium-ion battery anodes with a long cycling life. Nanoscale 2013;5(10):4186-90.

[20] Tan GQ, Wu F, Yuan YF, et al. Freestanding three-dimensional core-shell nanoarrays for lithium-ion battery anodes. Nat Commun 2016;7:11774.

[21] Liu WB, Cheng P, Yan XM, et al. Facile one-step solution-phase route to synthesize hollow nanoporous Cu_xO microcages on 3D copper foam for superior Li storage. ACS Sustain Chem Eng https://doi.org/10.1021/acssuschemeng.0c09203.

[22] Zhu CR, Chao DL, Sun J, et al. Enhanced lithium storage performance of CuO nanowires by coating of graphene quantum dots. Adv Mater Interfaces 2015;2(2):239-45.

[23] Jeong JM, Choi BG, Lee SC, et al. Hierarchical hollow spheres of Fe_2O_3@Polyaniline for lithium ion battery anodes. Adv Mater 2013;25(43):6250-5.

[24] Yun QB, He YB, Lv W, et al. Chemical dealloying derived 3D porous current collector for Li metal anodes. Adv Mater 2016;28(32):6932-9.

[25] Liu WB, Chen X, Zhang JZ, et al. In-situ synthesis of freestanding porous SnO_x-decorated Ni_3Sn_2 composites with enhanced Li storage properties. Chem Eng J 2021;412:128591.

[26] Yu Y, Gu L, Lang XY, et al. Li storage in 3D nanoporous Au-supported nanocrystalline tin. Adv Mater 2011;23(21):2443-7.

[27] Liu WB, Zhang SC, Li N, et al. Facile one-pot synthesis of nanoporous copper ribbons with bimodal pore size distributions by chemical dealloying. J Electrochem Soc 2011;158(10):D611-5.

[28] Liu WB, Zhang SC, Li N, et al. Influence of dealloying solution on the microstructure of monolithic nanoporous copper through chemical dealloying of Al 30

at.% Cu alloy. Int J Electrochem Sci 2012;7(9):7993-8006.

[29] Zhang XM, Li YX, Liu Y, et al. Fabrication of a bimodal micro/nanoporous metal by the gasar and dealloying processes. Mater Lett 2013;92:448-51.

[30] Dong X, Liu WB, Chen X, et al. Novel three dimensional hierarchical porous Sn-Ni alloys as anode for lithium ion batteries with long cycle life by pulse electrodeposition. Chem Eng J 2018;350:791-8.

[31] Liu WB, Chen L, Cui L, et al. Freestanding 3D nanoporous Cu@1D Cu_2O nanowire heterostructure: from facile one-step protocol to robust application in Li storage. J Mater Chem A 2019;7(25):15089-100.

[32] Liu RQ, Lia DY, Wang C, et al. Core–shell structured hollow SnO_2–polypyrrole nanocomposite anodes with enhanced cyclic performance for lithium-ion batteries. Nano Energy 2014;6:73-81.

[33] Xu WW, Zhao KN, Niu CJ, et al. Heterogeneous branched core–shell SnO_2–PANI nanorod arrays with mechanical integrity and three dimentional electron transport for lithium batteries. Nano Energy 2014;8:196-204.

[34] Ding HM, Jiang H, Zhu ZJ, et al. Ternary SnO_2@PANI/rGO nanohybrids as excellent anode materials for lithium-ion batteries. Electrochim Acta 2015;157:205-10.

[35] Wu H, Yu GH, Pan LJ, et al. Stable Li-ion battery anodes by in-situ polymerization of conducting hydrogel to conformally coat silicon nanoparticles. Nat Commun 2013;4:1943.

[36] Erlebacher J. An atomistic description of dealloying. J Electrochem Soc

2004;151(10):C614-26.

[37] Liu WB, Cheng P, Zhang SC, et al. Facile in-situ synthesis of freestanding 3D nanoporous Cu@Cu_2O hierarchical nanoplate arrays as binder-free integrated anodes for high-capacity, long-life Li-ion batteries. Metall Mater Trans A 2020;51(5):2536-48.

[38] Paolella A, Brescia R, Prato M, et al. Colloidal synthesis of cuprite (Cu_2O) octahedral nanocrystals and their electrochemical lithiation. ACS Appl Mater Interfaces 2013;5(7):2745-51.

[39] Ghijsen J, Tjeng LH, Elp JV, et al. Electronic structure of Cu_2O and CuO. Phys Rev B 1988;38(16):11322.

[40] Wu SH, Fu GL, Lv WQ, et al. A single-step hydrothermal route to 3D hierarchical Cu_2O/CuO/rGO nanosheets as high-performance anode of lithium-ion batteries. Small 2018;14(5):1870020.

[41] Debbichi L, Marco de Lucas MC, Pierson JF, et al. Vibrational properties of CuO and Cu_4O_3 from first-principles calculations, and raman and infrared spectroscopy. J Phys Chem C 2012;116(18):10232-7.

[42] Drury A, Chaure S, Kroll M, et al. Fabrication and characterization of silver/polyaniline composite nanowires in porous anodic alumina. Chem Mater 2007;19(17):4252-8.

[43] Laruelle S, Grugeon S, Poizot P, et al. On the Origin of the Extra Electrochemical Capacity Displayed by MO/Li Cells at Low Potential. J Electrochem Soc 2002;149(5):A627-34.

[44] Wang GX, Sui YM, Zhang MN, et al. One-pot synthesis of uniform Cu_2O-CuO-TiO_2 hollow nanocages and highly stable lithium storage properties. J Mater Chem A 2017;5(35):18577-84.

[45] Shin JH, Park SH, Hyun SM, et al. Electrochemical flow-based solution-solid growth of the Cu_2O nanorod array: potential application to lithium ion batteries. Phys Chem Chem Phys 2014;16(34):18226-32.

[46] Li N, Xiao Y, Hu CW, et al. Microwave-assisted synthesis of dual-conducting Cu_2O@Cu-graphene system with improved electrochemical performance as anode material for lithium batteries. Chem-Asian J 2013;8(9):1960-5.

[47] Li N, Xiao Y, Hu CW, et al. Investigation of the role of Cu_2O beads over the wrinkled graphene as an anode material for lithium ion battery. Int J Hydrogen Energy 2016;41(6):3974-80.

[48] Wu H, Zheng G, Liu N, et al. Engineering empty space between Si nanoparticles for lithium-ion battery anodes. Nano Lett 2012;12(2):904-9.

[49] Chao DL, Liang P, Chen Z, et al. Pseudocapacitive Na-ion storage boosts high rate and areal capacity of self-branched 2D layered metal chalcogenide nanoarrays. ACS Nano 2016;10(11) :10211-9.

[50] Lukatskaya MR, Kota S, Lin ZF, et al. Ultra-high-rate pseudocapacitive energy storage in two-dimensional transition metal carbides. Nat Energy 2017;2(8) :17105

[51] Wang J, Polleux J, Lim J, et al. Pseudocapacitive contributions to electrochemical energy storage in TiO_2 (Anatase) nanoparticles. J Phys Chem C 2007;111(40) :14925-31.

[52] Tang QM, Cui YH, Wu JW, et al. Ternary tin selenium sulfide ($SnSe_{0.5}S_{0.5}$) nano alloy as the high-performance anode for lithium-ion and sodium-ion batteries. Nano Energy 2017;41:377-86.

[53] Hu, XJ, Liu XJ, Chen K, et al. Core-shell MOF-derived N-doped yolk-shellcarbon nanocages homogenously filled with ZnSe and $CoSe_2$ nanodots as excellent anode materials for lithium- and sodium-ion batteries. J Mater Chem A 2019;7(18):11016-37.

[54] Liu YH, Yu XY, Fang YJ, et al. Confining SnS_2 ultrathin nanosheetsin hollow carbon nanostructures for efficient capacitive sodium storage. Joule 2018;2(4):725-35.

[55] Tan YZ, Wong KW, Ng KM. Novel silicon doped tin oxide-carbon microspheres as anode material for lithium ion batteries: the multiple effects exerted by doped Si. Small 2017;13(48):1702614.

[56] Wang YK, Zhang HY, Hu RZ, et al. Fe_3O_4/SnO_2/rGO ternary composite as a high-performance anode material for lithium-ion batteries. J Alloys Compd 2017;693:1174-9.

[57] Zhang HG, Yu XD, Braun PV. Three-dimensional bicontinuous ultrafast-charge and -discharge bulk battery electrodes. Nat Nanotechnol 2011;6(5):277-81.

[58] Cui LF, Yang Y, Hsu CM, et al. Carbon-silicon core-shell nanowires as high capacity electrode for lithium ion batteries. Nano Lett 2009;9(9):3370-4.

[59] Bao LH, Zang JF, Li XD. Flexible Zn_2SnO_4/MnO_2 core/shell nanocable-carbon microfiber hybrid composites for high-performance supercapacitor electrodes. Nano

Lett 2011;11(3):1215-20.

[60] Wang Z, Zhang X, Yan Y, et al. Nanoporous GeO_2/Cu/Cu_2O network synthesized by dealloying method for stable Li-ion storage. Electrochim Acta 2019;300:363-72.

Figure Captions

Figure 1. (a) Schematic of preparation process of 3D-CBS NPC@Cu_2O@PANI electrode. Planar and cross-section SEM images of (b-c) 3D-CS NPC@Cu_2O and (d-e) 3D-CBS NPC@Cu_2O@PANI electrodes, in which the upper-right insets are their corresponding low-magnification SEM images, and the bottom-left insets in parts b and d are typical digital photographs of 3D-CS NPC@Cu_2O and 3D-CBS NPC@Cu_2O@PANI electrodes. (HR)TEM images of (f-g) 3D-CS NPC@Cu_2O and (h) 3D-CBS NPC@Cu_2O@PANI electrodes, in which the upper-right insets in parts f and g are the corresponding high-magnification TEM image and SAED pattern, respectively.

Figure 2. (a) XRD patterns of the as-cast $Cu_{65}Sn_{35}$ alloy, as-synthesized 3D-CS NPC@Cu_2O and 3D-CBS NPC@Cu_2O@PANI electrodes. (b) XPS survey spectra and (c) Cu 2p high-resolution XPS spectra of 3D-CS NPC@Cu_2O and 3D-CBS NPC@Cu_2O@PANI electrodes. (d) Raman spectra of 3D-CS NPC@Cu_2O and 3D-CBS NPC@Cu_2O@PANI electrodes.

Figure 3. (a) CVs of 3D-CBS NPC@Cu_2O@PANI electrode recorded at a scan rate of 0.1 mV s^{-1} between 0.01-3.0 V (vs. Li/Li^+). (b) Potential vs. capacity profiles of 3D-CBS NPC@Cu_2O@PANI electrode for 1^{st}, 2^{nd}, 3^{rd}, 4^{th} and 100^{th} cycles. (c) Cycle performance of 3D-CS NPC@Cu_2O and 3D-CBS NPC@Cu_2O@PANI electrodes at a current density of 2 A g^{-1}. (d-e) Long-cycle galvanostatic charge-discharge curves of 3D-CBS NPC@Cu_2O@PANI electrode at higher current densities of 4 and 6 A g^{-1}, respectively. (f) Rate capability of 3D-CBS NPC@Cu_2O@PANI electrode designed at

different current densities involving 5 multistep-rate periods from 2 up to 20 A g^{-1} and back to 2 A g^{-1} repeatedly. (g) Potential vs. capacity profiles of 3D-CBS NPC@Cu_2O@PANI electrode at the current density of 20 A g^{-1} designed in each multistep-rate period. (h) Scattergram of reversible specific capacity vs. cycle number at the lowest (2 A g^{-1}) and highest (20 A g^{-1}) current densities designed in each multistep-rate period, respectively. (i) Integration of rate capability of 3D-CBS NPC@Cu_2O@PANI electrode at different current densities with subsequent cycle performance at the fixed high current density. (j) Scattergram of comparison of cycle performance of various Cu-based oxides and their composites at different current densities marked in the brackets. The detailed experiment data and related references are listed in Table S1.

Figure 4. (a) CVs of 3D-CBS NPC@Cu_2O@PANI electrode at different scan rates from 0.2 to 3.0 mV s^{-1}. (b) Plots (b values) of the log(scan rate) *versus* log(peak current) at different oxidation and reduction states. (c) Ratio of capacitive-controlled charge contribution (grey) to the total current at a scan rate of 2.0 mV s^{-1}. (d) Ratio of capacitive and diffusion-controlled contribution to Li^+ charge storage at different scan rates.

Figure 5. (a-b) Nyquist plots of 3D-CS NPC@Cu_2O and 3D-CBS NPC@Cu_2O@PANI electrodes before and after cycling. (c-d) Relations between Z' and $\omega^{-1/2}$ in low frequency ranges of EIS for 3D-CS NPC@Cu_2O and 3D-CBS NPC@Cu_2O@PANI electrodes.

Figure 6. SEM images of (a) 2D CF@Cu_2O NPs, (b) 3D-CS NPC@Cu_2O and (c)

3D-CBS NPC@Cu_2O@PANI electrodes after 300 charge-discharge cycles at a current density of 2 A g^{-1}, respectively. (d) SEM images of 3D-CBS NPC@Cu_2O@PANI electrode after 11500 ultralong-cycles at a current density of 6 A g^{-1}. Insets are their corresponding high-magnification SEM images.

Figure 7. (a) Cycle performance curves with intermittent rate measurements of 3D-CBS NPC@Cu_2O@PANI//$LiCoO_2$ full cell. (b-d) Enlarged intermittent rate capability profiles of 3D-CBS NPC@Cu_2O@PANI//$LiCoO_2$ full cell recorded from the 1^{st} to 50^{th} cycles, from the 1040^{th} to 1090^{th} cycles, and from the 2080^{th} to 2130^{th} cycles, respectively. (e-h) Voltage vs. capacity profiles of 3D-CBS NPC@Cu_2O@PANI//$LiCoO_2$ full cell at different current densities. (i) Typical digital photograph of LED bulb lightened by the assembled full cell with full-charged state after 3000 charge-discharge cycles.

Figure 8. (a) Schematic illustration for lithiation-delithiation reaction of 3D-CBS NPC@Cu_2O@PANI electrode. (b) DFT simulation of 3D and 2D surface atomic configurations in different planes of Cu_2O. E_s refers to surface energy.

Table 1. The Li^+ diffusion coefficients of 3D-CBS NPC@Cu_2O@PANI and 3D-CS NPC@Cu_2O electrodes before and after cycling estimated by Eqn. (3).

Specimen / State	3D-CBS NPC@Cu_2O@PANI electrode ($\times10^{-11}$ cm^2 s^{-1})	3D-CS NPC@Cu_2O electrode ($\times10^{-11}$ cm^2 s^{-1})
Before cycling	5.52	1.29
After 300 cycles	24.20	0.15
After 11500 cycles	1.77	/

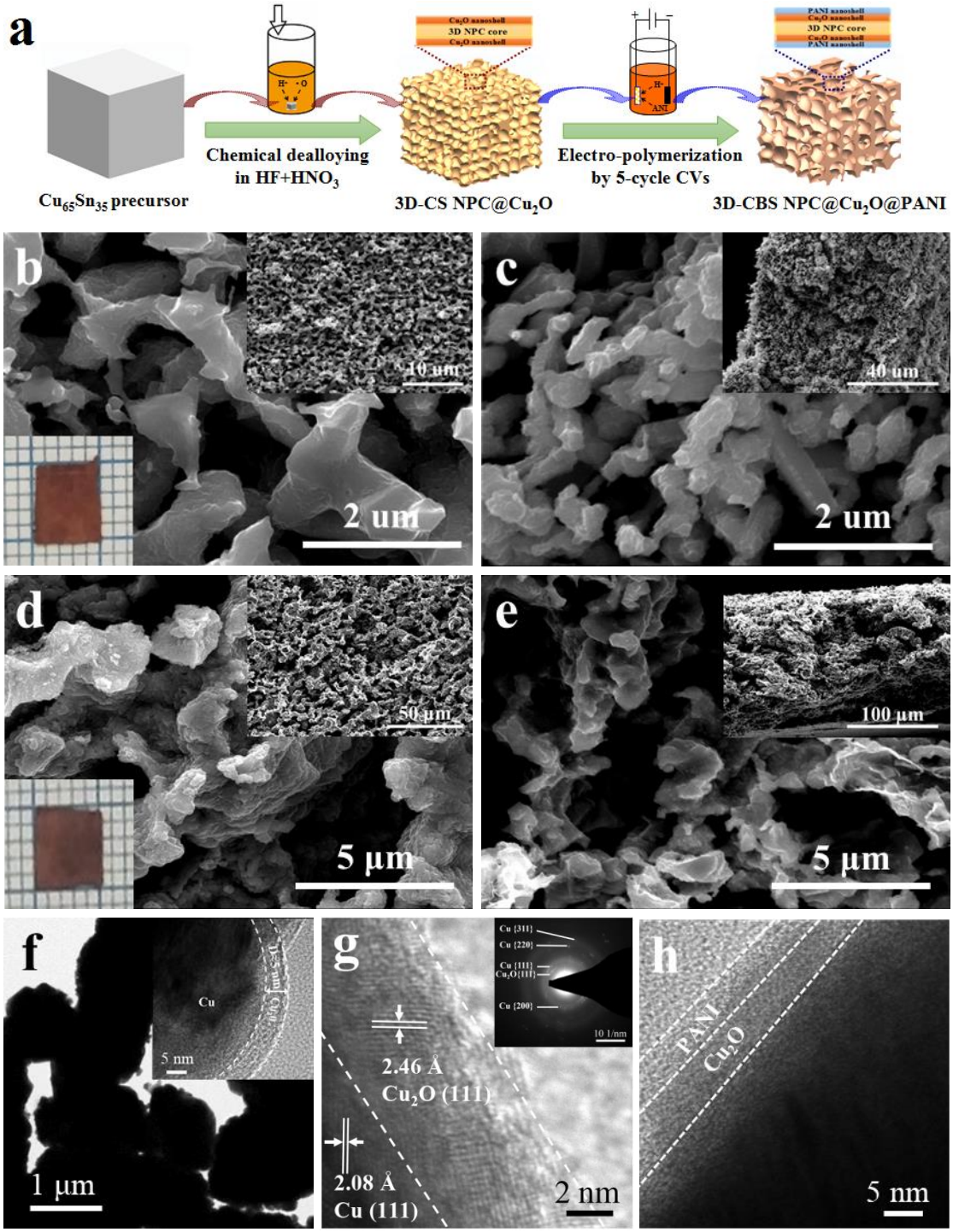

Figure 1. (a) Schematic of preparation process of 3D-CBS NPC@Cu_2O@PANI electrode. Planar and cross-section SEM images of (b-c) 3D-CS NPC@Cu_2O and (d-e) 3D-CBS NPC@Cu_2O@PANI electrodes, in which the upper-right insets are their corresponding low-magnification SEM images, and the bottom-left insets in parts b and d are typical digital photographs of 3D-CS NPC@Cu_2O and 3D-CBS NPC@Cu_2O@PANI electrodes. (HR)TEM images of (f-g) 3D-CS NPC@Cu_2O and (h) 3D-CBS NPC@Cu_2O@PANI electrodes, in which the upper-right insets in parts f and g are the corresponding high-magnification TEM image and SAED pattern, respectively.

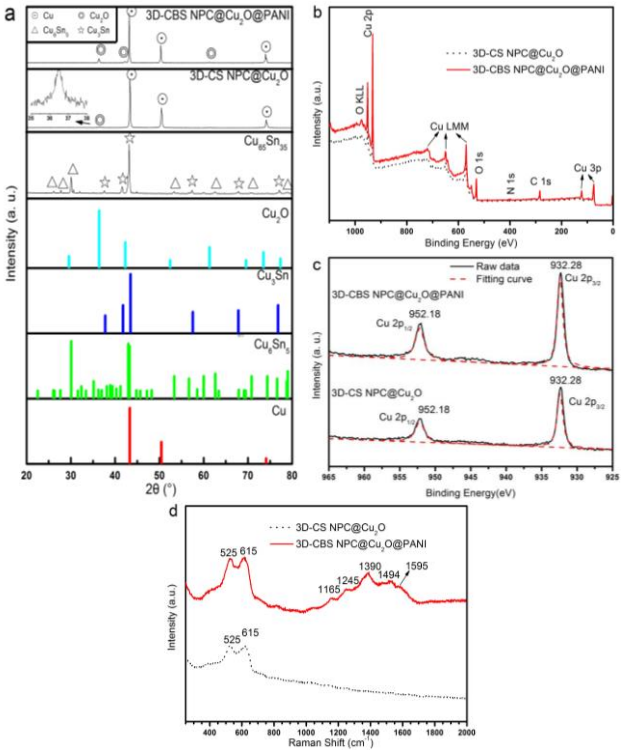

Figure 2. (a) XRD patterns of the as-cast $Cu_{65}Sn_{35}$ alloy, as-synthesized 3D-CS NPC@Cu_2O and 3D-CBS NPC@Cu_2O@PANI electrodes. (b) XPS survey spectra and (c) Cu 2p high-resolution XPS spectra of 3D-CS NPC@Cu_2O and 3D-CBS NPC@Cu_2O@PANI electrodes. (d) Raman spectra of 3D-CS NPC@Cu_2O and 3D-CBS NPC@Cu_2O@PANI electrodes.

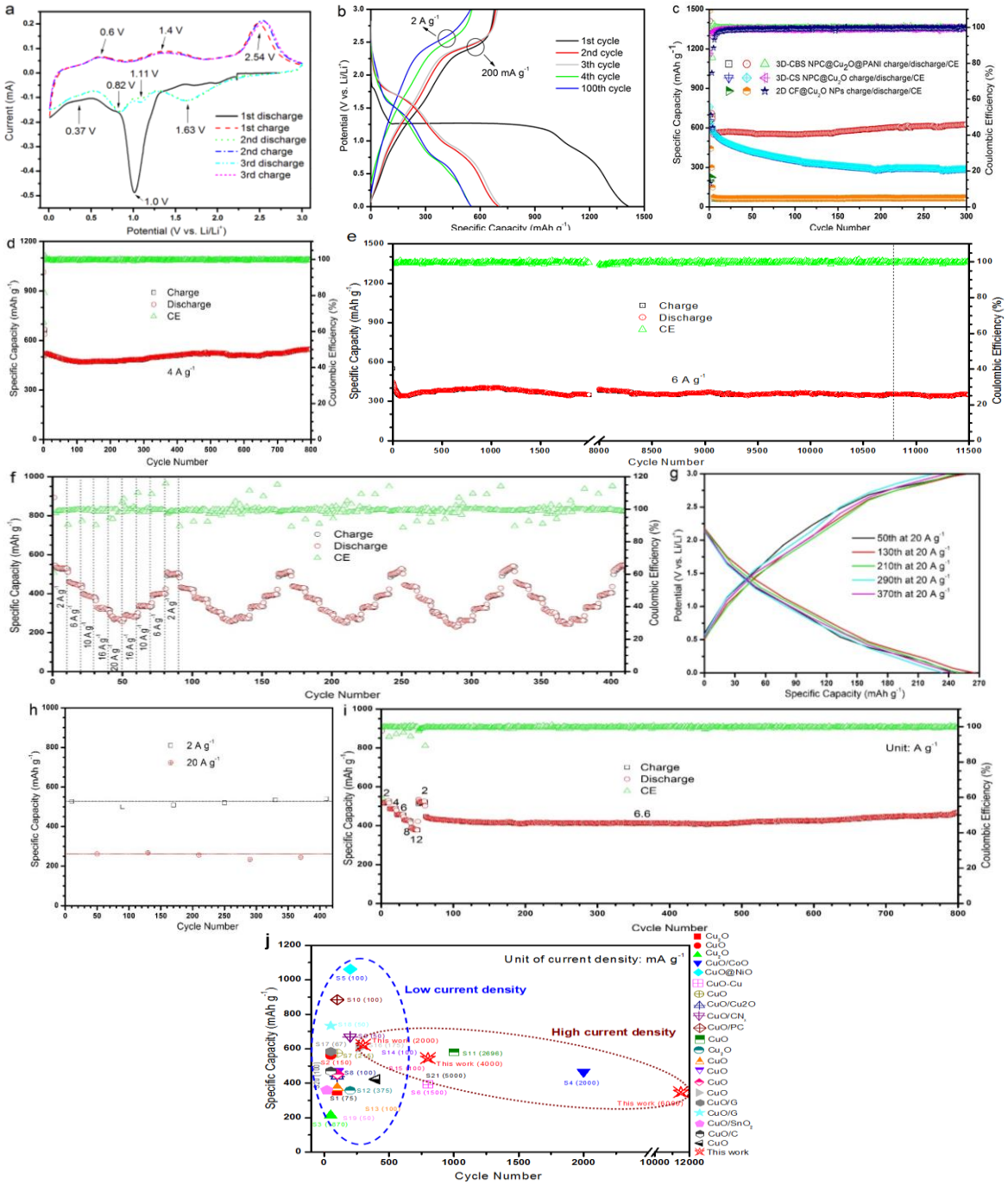

Figure 3. (a) CVs of 3D-CBS NPC@Cu_2O@PANI electrode recorded at a scan rate of 0.1 mV s^{-1} between 0.01-3.0 V (vs. Li/Li^+). (b) Potential vs. capacity profiles of 3D-CBS NPC@Cu_2O@PANI electrode for 1st, 2nd, 3rd, 4th and 100th cycles. (c) Cycle performance of 3D-CS NPC@Cu_2O and 3D-CBS NPC@Cu_2O@PANI electrodes at a current density of 2 A g^{-1}. (d-e) Long-cycle galvanostatic charge-discharge curves of 3D-CBS NPC@Cu_2O@PANI electrode at higher current densities of 4 and 6 A g^{-1}, respectively. (f) Rate capability of 3D-CBS NPC@Cu_2O@PANI electrode designed at different current densities involving 5 multistep-rate periods from 2 upto 20 A g^{-1} and back to 2 A g^{-1} repeatedly. (g) Potential vs. capacity profiles of 3D-CBS NPC@Cu_2O@PANI electrode at the current density of 20 A g^{-1} designed in each multistep-rate period. (h) Scattergram of reversible specific capacity vs. cycle number

at the lowest (2 A g^{-1}) and highest (20 A g^{-1}) current densities designed in each multistep-rate period, respectively. (i) Integration of rate capability of 3D-CBS NPC@Cu_2O@PANI electrode at different current densities with subsequent cycle performance at the fixed high current density. (j) Scattergram of comparison of cycle performance of various Cu-based oxides and their composites at different current densities marked in the brackets. The detailed experiment data and related references are listed in Table S1.

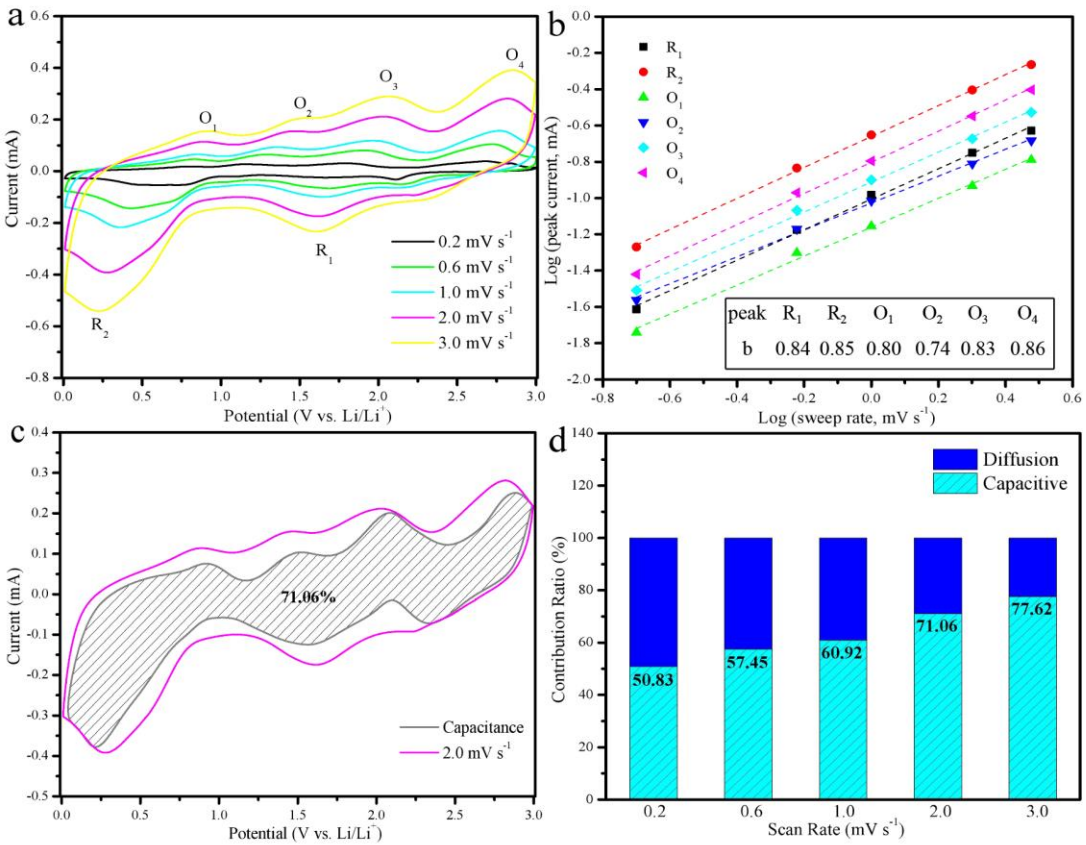

Figure 4. (a) CVs of 3D-CBS NPC@Cu_2O@PANI electrode at different scan rates from 0.2 to 3.0 mV s^{-1}. (b) Plots (b values) of the log(scan rate) *versus* log(peak current) at different oxidation and reduction states. (c) Ratio of capacitive-controlled charge contribution (grey) to the total current at a scan rate of 2.0 mV s^{-1}. (d) Ratio of capacitive- and diffusion-controlled contribution to Li^+ charge storage at different scan rates.

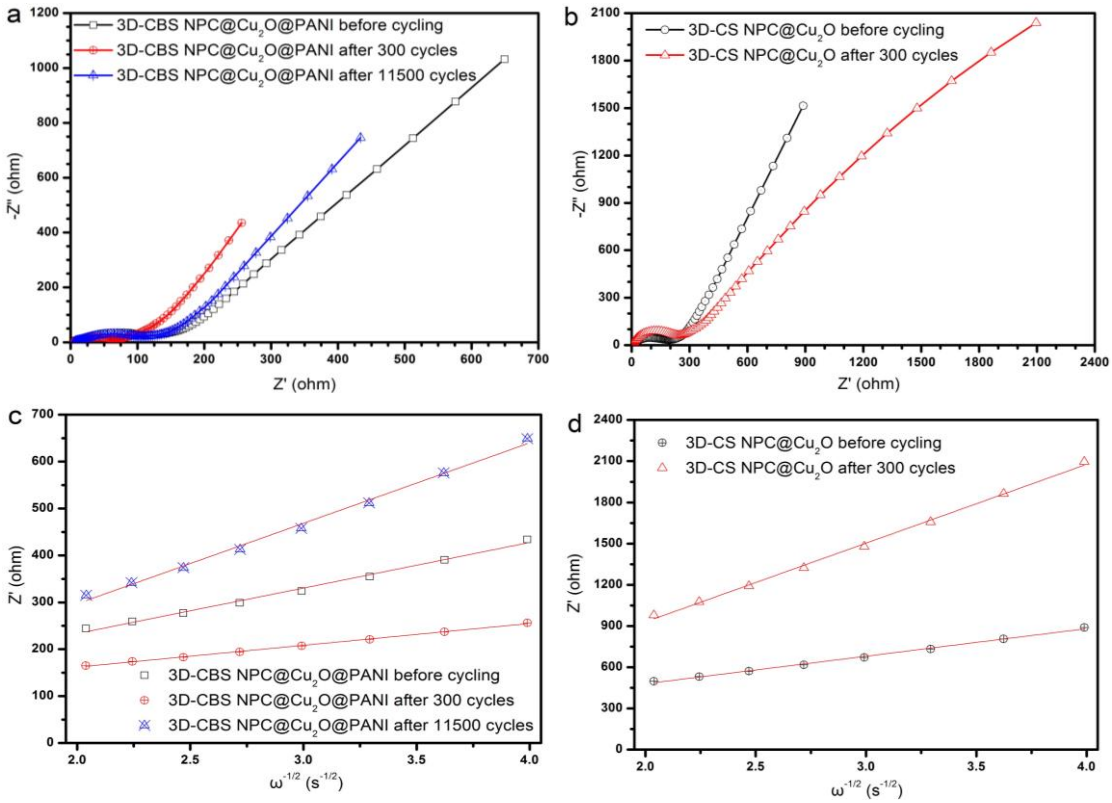

Figure 5. (a-b) Nyquist plots of 3D-CS NPC@Cu_2O and 3D-CBS NPC@Cu_2O@PANI electrodes before and after cycling. (c-d) Relations between Z' and $\omega^{-1/2}$ in low frequency ranges of EIS for 3D-CS NPC@Cu_2O and 3D-CBS NPC@Cu_2O@PANI electrodes.

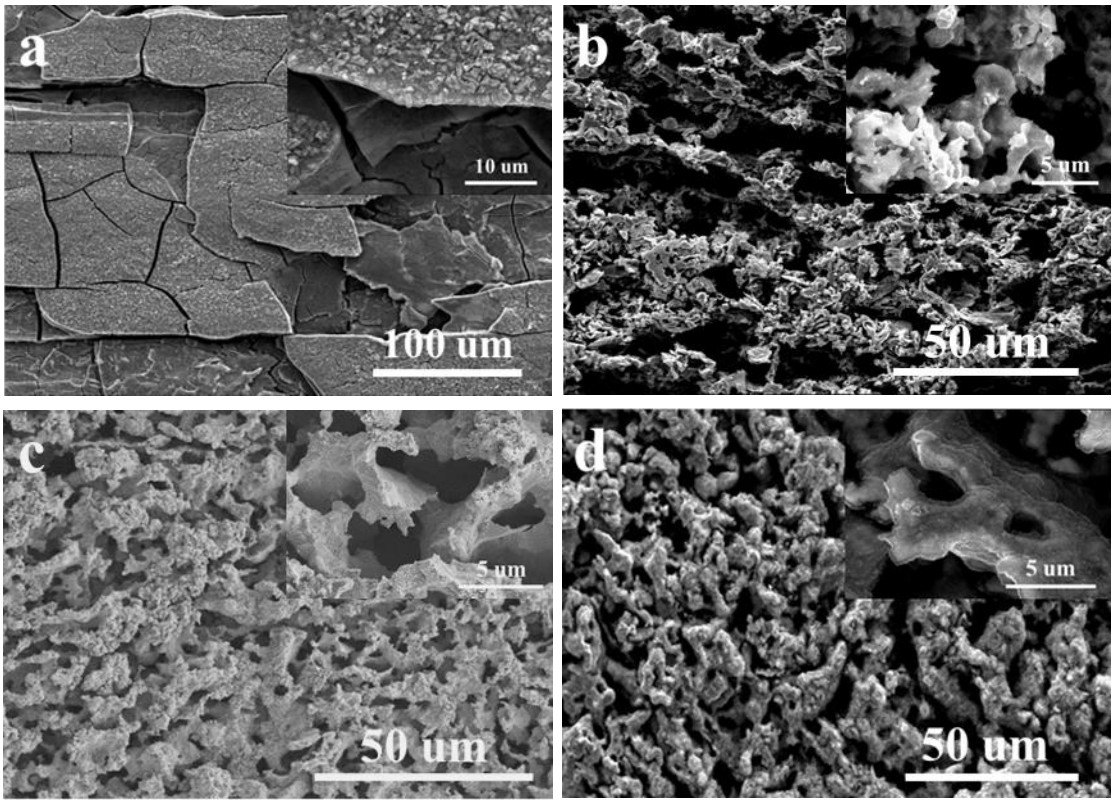

Figure 6. SEM images of (a) 2D CF@Cu_2O NPs, (b) 3D-CS NPC@Cu_2O and (c) 3D-CBS NPC@Cu_2O@PANI electrodes after 300 charge-discharge cycles at a current density of 2 A g^{-1}, respectively. (d) SEM images of 3D-CBS NPC@Cu_2O@PANI electrode after 11500 ultralong-cycles at a current density of 6 A g^{-1}. Insets are their corresponding high-magnification SEM images.

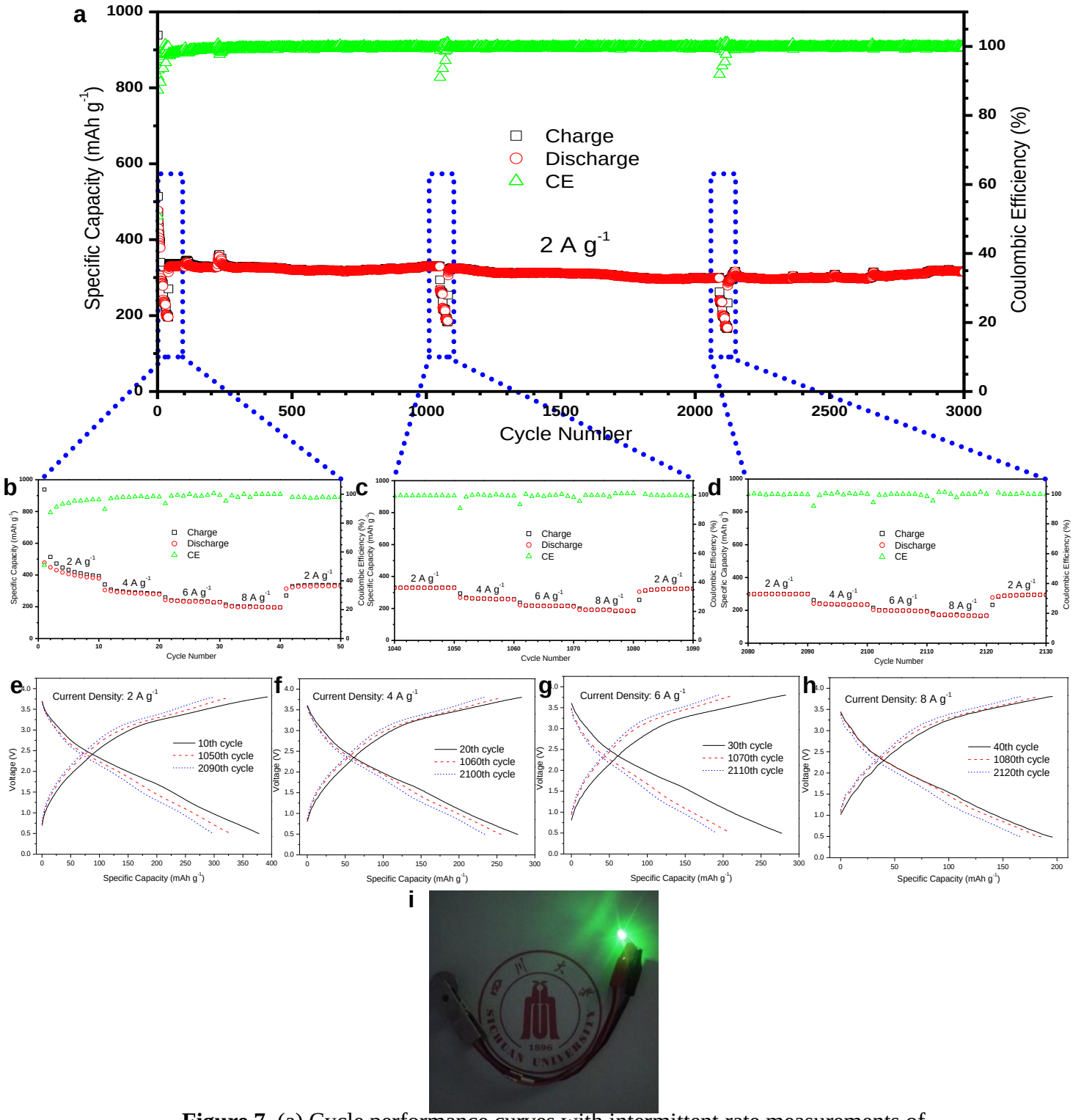

Figure 7. (a) Cycle performance curves with intermittent rate measurements of 3D-CBS NPC@Cu_2O@PANI//$LiCoO_2$ full cell. (b-d) Enlarged intermittent rate capability profiles of 3D-CBS NPC@Cu_2O@PANI//$LiCoO_2$ full cell recorded from the 1st to 50th cycles, from the 1040th to 1090th cycles, and from the 2080th to 2130th cycles, respectively. (e-h) Voltage vs. capacity profiles of 3D-CBS NPC@Cu_2O@PANI//$LiCoO_2$ full cell at different current densities. (i) Typical digital photograph of LED bulb lightened by the assembled full cell with full-charged state after 3000 charge-discharge cycles.

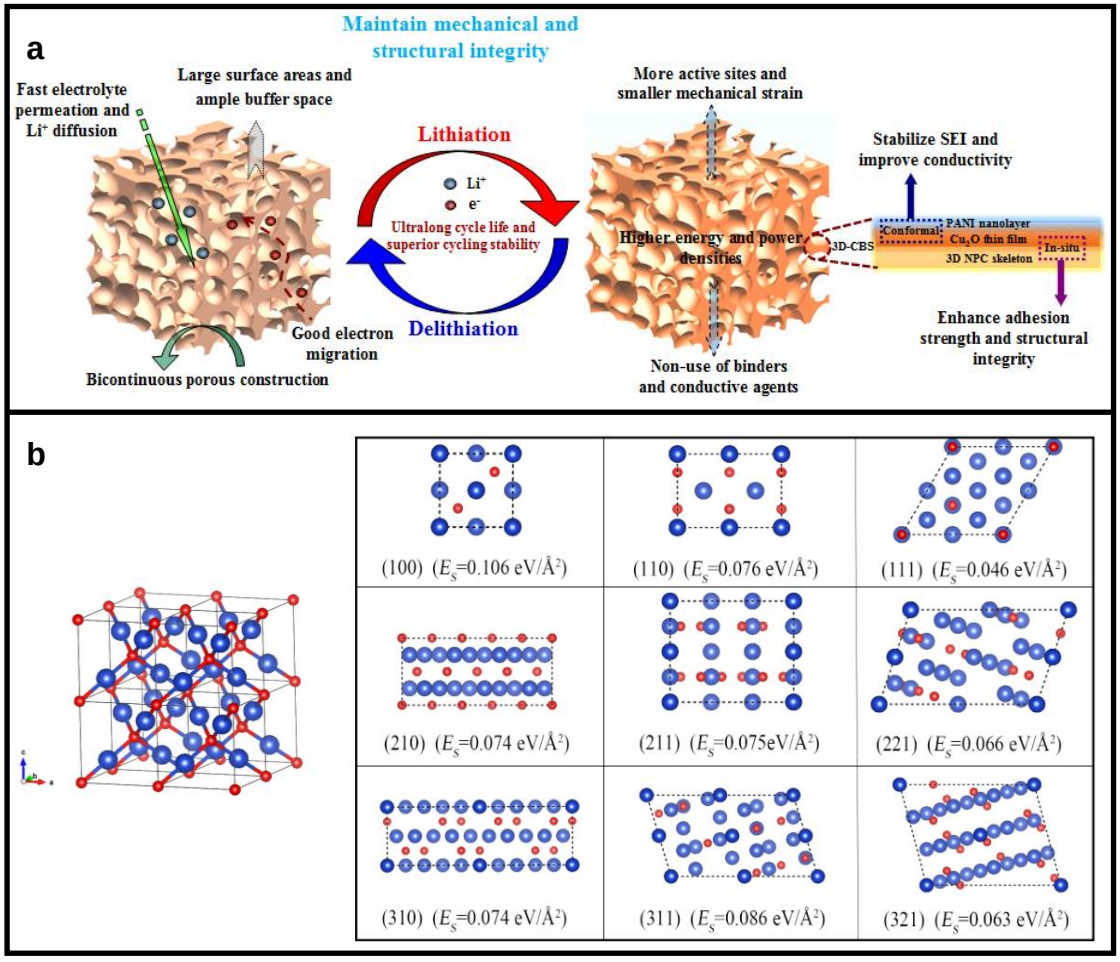

Figure 8. (a) Schematic illustration for lithiation-delithiation reaction of 3D-CBS NPC@Cu_2O@PANI electrode. (b) DFT simulation of 3D and 2D surface atomic configurations in different planes of Cu_2O. E_s refers to surface energy.